Supplementary information

Crystal Engineering of Manganese Nitride Thin Film Electrodes for All-Nitride Asymmetric Supercapacitors

Quanxing Guo,[a] Shuyue Fang,[a] Binbin Wei,[a,b]* Qiaoyan Chen,[a] Junjie Chen,[a] Junhong Huang,[a] Jingang Wu,[a] Minming Jiang,[a]* Xiaohong Ge,[d] Ningbo Liao,[e] Hanfeng Liang,[c] and Zhengbing Qi[a]*

[a]*Key Laboratory of Functional Materials and Applications of Fujian Province, School of Materials Science and Engineering, Xiamen University of Technology, Xiamen, 361024, China*

[b]*Department of Materials Science and Engineering, National University of Singapore, Singapore, 117574, Singapore*

[c]*State Key Laboratory of Physical Chemistry of Solid Surfaces, Tan Kah Kee Innovation Laboratory (IKKEM), College of Chemistry and Chemical Engineering, Xiamen University, Xiamen, 361005, China*

[d]*Eyepol Optical Technology (Xiamen) Co., Ltd., Xiamen, 361009, China*

[e]*College of Mechanical & Electrical Engineering, Wenzhou University, Wenzhou, 325035, China*

*Corresponding author: bbwei@xmut.edu.cn (B.B. Wei), jiangminming@xmut.edu.cn (M.M. Jiang) and zbqi@xmut.edu.cn (Z.B. Qi)

Sputtering deposition of thin films

Manganese nitride and vanadium nitride thin films were deposited onto single-side polished silicon wafers (Hefei Kejing Materials Technology Co., Ltd, China) by reactive DC magnetron sputtering (Shenyang Keyi Co. Ltd, China) using high-purity Mn (99.5% purity, Jiangxi Ketai New Material Co. Ltd, China) and vanadium (99.9% purity, Jiangxi Ketai New Material Co. Ltd, China) targets, respectively. Prior to deposition, the silicon substrates were sequentially ultrasonically cleaned in acetone and alcohol for 10 min each, and then placed into the vacuum chamber. During the sputtering process of both manganese nitride and vanadium nitride thin films, the base pressure and working pressure were kept constant at 6×10^{-4} Pa and 3.0 Pa, respectively. The crystal structure and thickness of manganese nitride thin films (i.e. cubic Mn_4N, hexagonal Mn_2N, and tetragonal Mn_3N_2) was regulated by varying the N_2 flow rate (2.5, 5, and 10 sccm) and the deposition time (25, 30 and 35 min) while maintaining a constant total gas flow rate of 50 sccm and a sputtering power of 60 W. For the vanadium nitride (VN) thin films, the N_2 flow rates were set to 5, 7.5, and 10 sccm at a total gas flow rate of 50 sccm. And the deposition time was maintained at 30 min, with a sputtering power of 200 W.

Structural and morphological characterizations

The phase structures of thin films were investigated by X-ray diffraction (XRD, Rigaku Ultima IV, Japan) with Cu *K*α radiation. The surface composition and electronic states were analyzed by X-ray photoelectron spectroscopy (XPS, Axis Supra+, Japan) using monochromatic Al *K*α radiation (hv = 1486.6 eV). The surface and cross-sectional morphologies were examined by scanning electron microscopy (SEM, Zeiss Sigma, Germany). Transmission electron microscopy (TEM, FEI Talos F200s, USA), high-resolution TEM (HRTEM), selected-area electron diffraction (SAED), and energy-dispersive X-ray spectroscopy (EDS) elemental mapping were further employed to investigate the microstructure, crystallinity, and elemental distribution.

Electrochemical characterizations

The supercapacitive performances of thin film electrodes were evaluated using the as-prepared thin films as the working electrodes, an Ag/AgCl (Gaoss Union Technology Co., Ltd, China) as the reference electrode, and a Pt foil (Gaoss Union Technology Co., Ltd, China) as the counter electrode in 1.0 M KOH. The asymmetric supercapacitor device was assembled by placing Mn_3N_2 and VN thin films in a

face-to-face configuration with a separator. Cyclic voltammetry at scan rates of 10, 20, 50 and 100 mV s^{-1}, galvanostatic charge-discharge (GCD) at current densities of 0.5, 1, 2 and 5 mA cm^{-2}, and electrochemical impedance spectroscopy (EIS) over a frequency range from 0.01 to 10^5 Hz with an AC amplitude of 5 mV were carried out on a CHI660E electrochemical workstation (Shanghai Chenhua Instrument Co. LTD, China). Long-term cycling tests of asymmetric supercapacitor device were performed for 20000 GCD cycles at a current density 5.0 mA cm^{-2}.

Electrochemical calculations

The specific areal capacitances (C_a, mF cm^{-2}) of thin film electrodes were calculated from the GCD curves using the following equation:

$$C_a = \frac{2I\int Udt}{SU^2\Big|_{U_1}^{U_2}}$$

The cell volumetric capacitances (C_{cell}, F cm^{-3}) of asymmetric supercapacitor device were computed by:

$$C_{cell} = \frac{2I\int Udt}{VU^2\Big|_{U_1}^{U_2}}$$

Where I is the discharge current, $\int Udt$ denotes the area under the discharge curve, S is the active electrode area, V is the device volume, and U_1 and U_2 are the initial and termination discharge voltages, respectively.

Energy density (E, mWh cm^{-3}) at different current densities was evaluated using the equation as follows:

$$E = \frac{1}{2\times 3.6} C_{cell}\Delta U^2$$

Similarly, power density (P, W cm^{-3}) was estimated by the following equation:

$$P = \frac{3.6\times E}{t}$$

where t is the discharging time, ΔU is the device voltage window.

Charge balance

To construct an asymmetric supercapacitor device, the charge balance between the positive (Mn_3N_2) and negative (VN) thin film electrodes should follow the relationship: $q^+ = q^-$. According to

$q=C_a \times \Delta U \times S$, the area ratio can be determined by:

$$\frac{S_{Mn_3N_2}}{S_{VN}} = \frac{\Delta U_{VN} \times C_{a,\,VN}}{\Delta U_{Mn_3N_2} \times C_{a,\,Mn_3N_2}} = \frac{141.8 \times 1}{76.6 \times 0.9} \approx \frac{2}{1}$$

Thus, an optimal areal ratio of 2:1 (Mn_3N_2:VN) was adopted to maximize the electrochemical performance of the asymmetric supercapacitor device.

DFT calculations

All calculations in this work were performed using the Cambridge Sequential Total Energy Package (CASTEP) code based on the density functional theory (DFT) method.[1] The exchange-correlation interactions between electrons were described by the generalized gradient approximation (GGA) with the Perdew-Burke-Ernzerhof (PBE) functional.[2,3] Ultrasoft pseudopotential was employed to handle electron-ion interactions.[4] The cutoff energy was set to 400 eV. The values of 1×10^{-5} eV and 0.03 eV/Å were selected as the convergence criteria for energy and force, respectively. For the bulk models, the k-point meshes for Mn_4N, Mn_2N and Mn_3N_2 were 6 × 6 × 6, 6 × 4 × 5 and 9 × 9 × 9, respectively. To account for the strongly correlated electrons, the U value of Mn 3d orbitals was set to 3.9 eV using the GGA+U method.[5] Based on the XRD results, the (111), (002) and (103) crystal planes of Mn_4N, Mn_2N and Mn_3N_2 were selected as the surface models for subsequent adsorption and diffusion, and all models considered the cases of N atoms and no N atoms on the surface. A 20 Å vacuum layer was introduced along the c-direction to avoid the effects of periodic mirroring. The Tkatchenko-Scheffler (TS) method was used to resolve the dispersive interactions between surface models and surface adsorbates.[6] The k-point meshes for Mn_4N (111), Mn_2N (002) and Mn_3N_2(103) surface models were all chosen as 4 × 4 × 1. The Mulliken charge population[7] and climbing-image nudged elastic band (CI-NEB) method[8] were used to characterize structural bonding characteristics, estimate the amount of charge transfer between adsorbed atoms and substrates, and calculate the diffusion barrier of K^+ on different surfaces, respectively. The adsorption energies (E_{ads}) of K^+ on different surfaces can be calculated according to the following formula:[9]

$$E_{ads} = E_{total} - \left(E_{surface} + E_{ion}\right)$$

where E_{total}, $E_{surface}$ and E_{ion} represent the total energy of the system after K^+ adsorption, the energy of the surface model, and the energy of a single K^+, respectively. According to this definition, a negative calculated value indicates that the adsorption process was exothermic (spontaneous).

Additional Figures and Tables

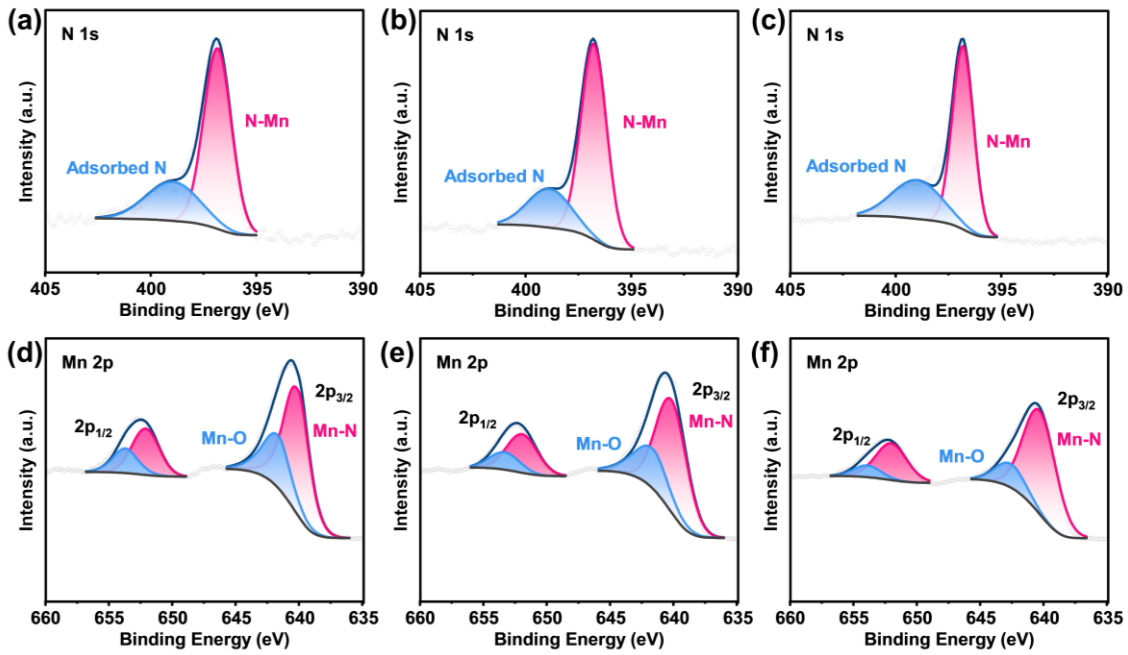

Fig. S1 XPS spectra of N 1*s* and Mn 2*p* for (a, d) Mn_4N, (b, e) Mn_2N, and (c, f) Mn_3N_2 thin films.

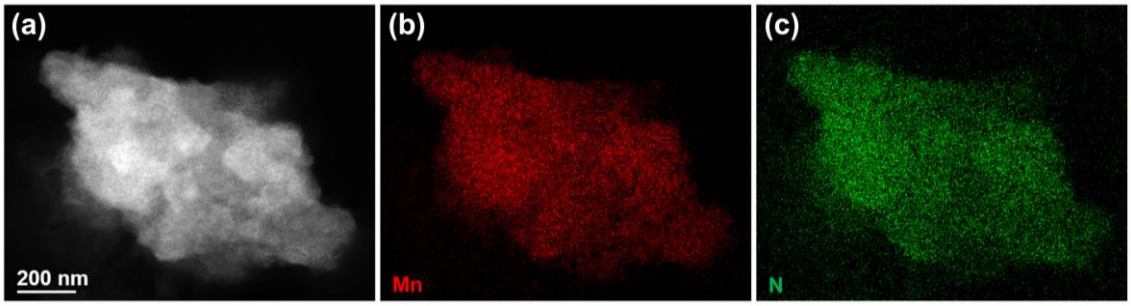

Fig. S2 EDS elemental mappings of Mn_3N_2 thin films.

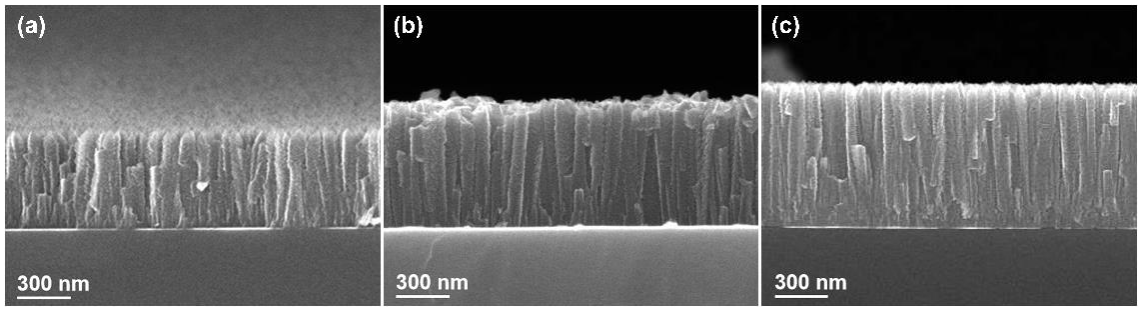

Fig. S3 Cross-sectional SEM images of Mn_3N_2 sputtered at the sputtering time of (a) 25, (b) 30 and (c) 35 min.

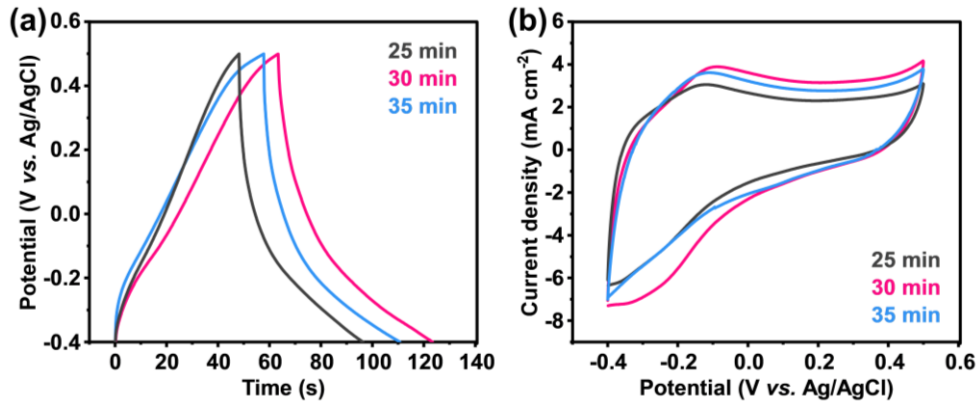

Fig. S4 Comparative GCD curves at 1.0 mA cm^{-2} and CV curves at 50 mV s^{-1} of Mn_3N_2 electrodes deposited at different sputtering times.

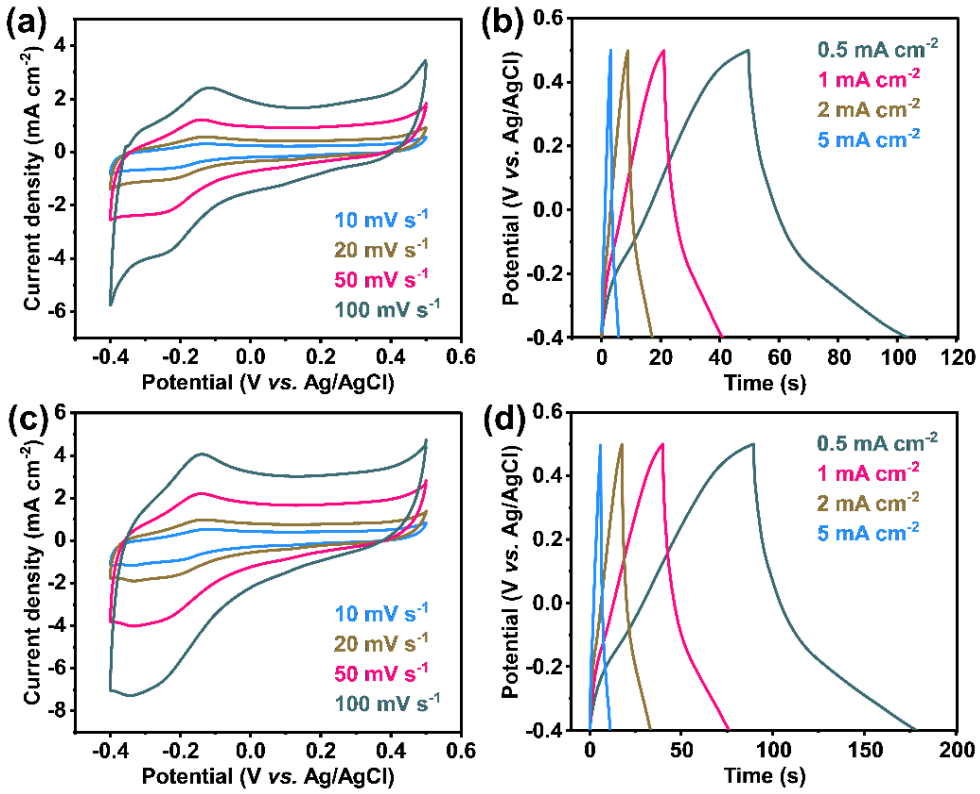

Fig. S5 CV curves at different scan rates and GCD curves at various current densities of (a, b) Mn_4N and (c, d) Mn_2N electrodes.

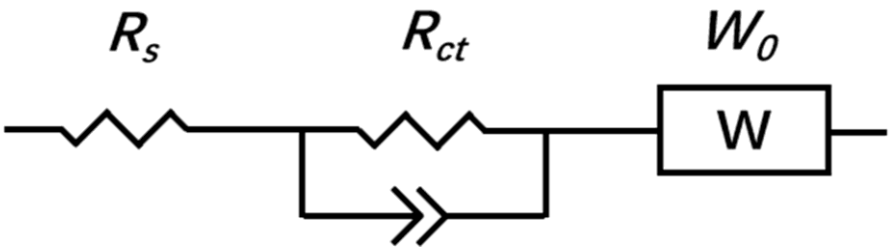

Fig. S6 The equivalent circuit model used for EIS fitting.

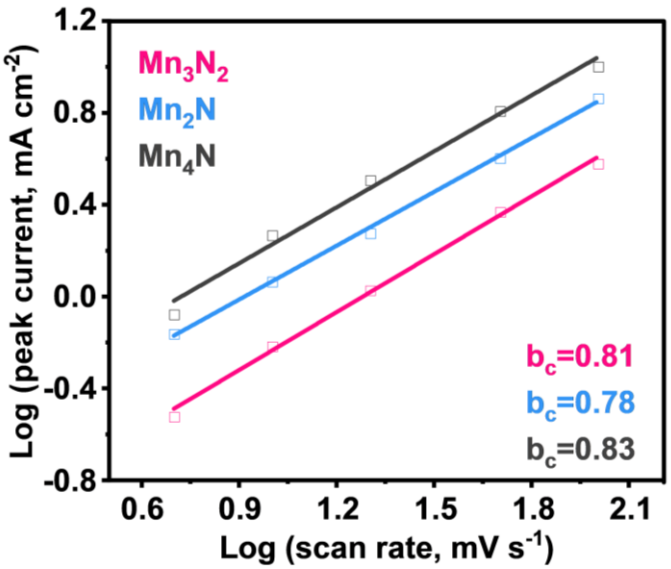

Fig. S7 b-values derived from cathodic scans.

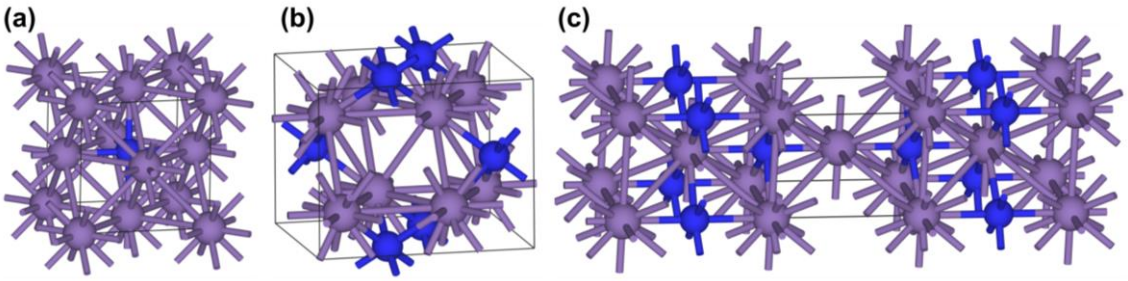

Fig. S8 Crystal structures of (a) Mn_4N, (b) Mn_2N and (c) Mn_3N_2.

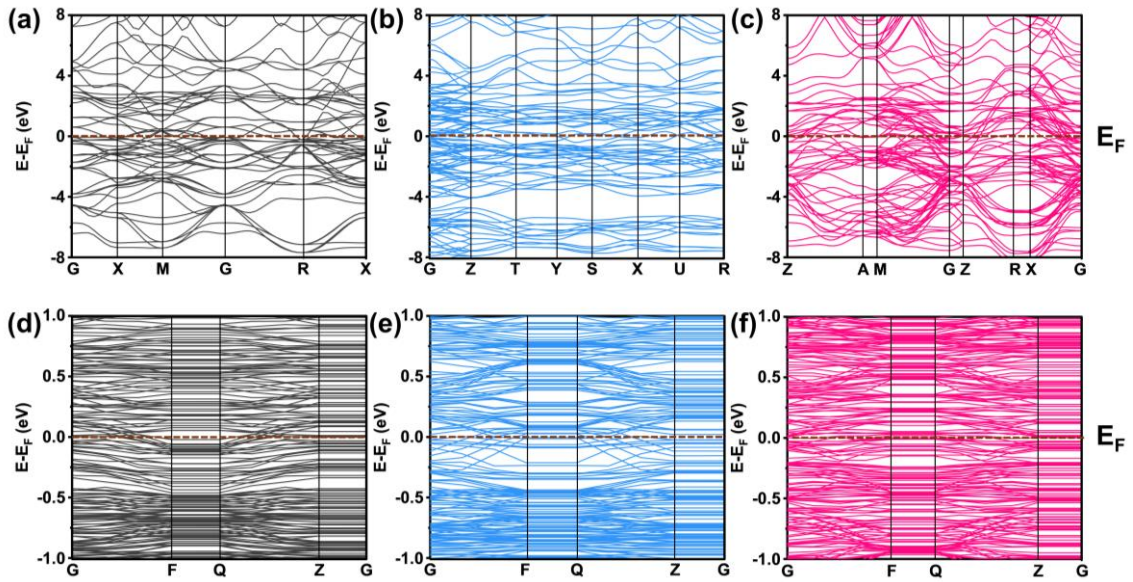

Fig. S9 Band structures of pristine and K^+ ions adsorption systems for (a, d) Mn_4N, (b, e) Mn_2N and (c, f) Mn_3N_2.

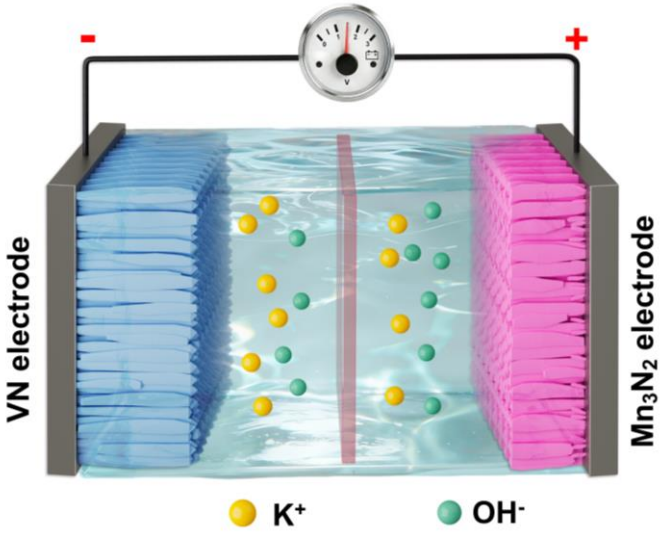

Fig. S10 Schematic illustration of Mn_3N_2//VN asymmetric supercapacitor device

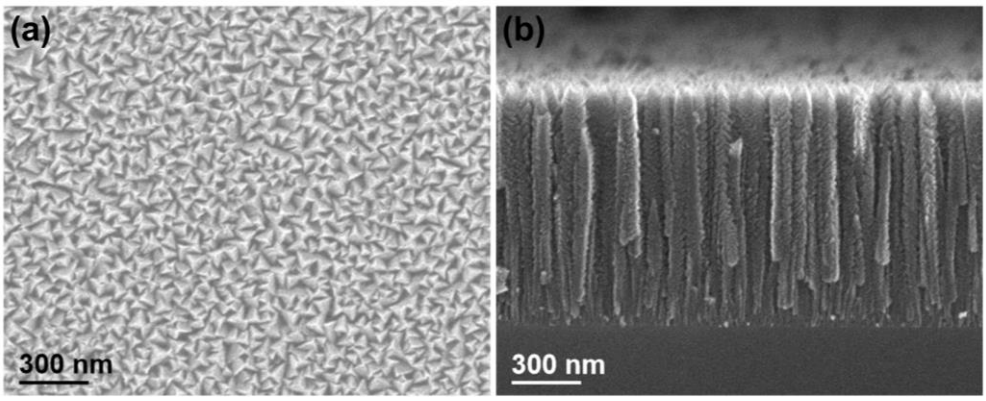

Fig. S11 (a) Surface and (b) cross-sectional SEM images of VN thin films sputtered at N_2 flow rate of 7.5 sccm.

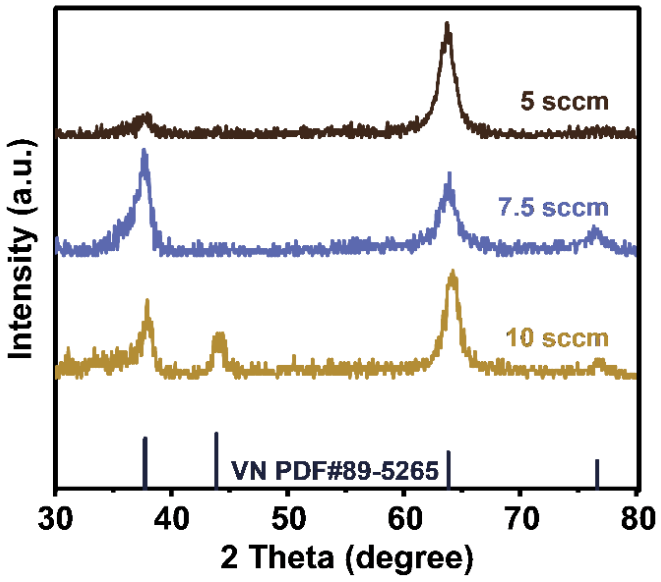

Fig. S12 XRD patterns of VN thin films deposited at different N_2 flow rates.

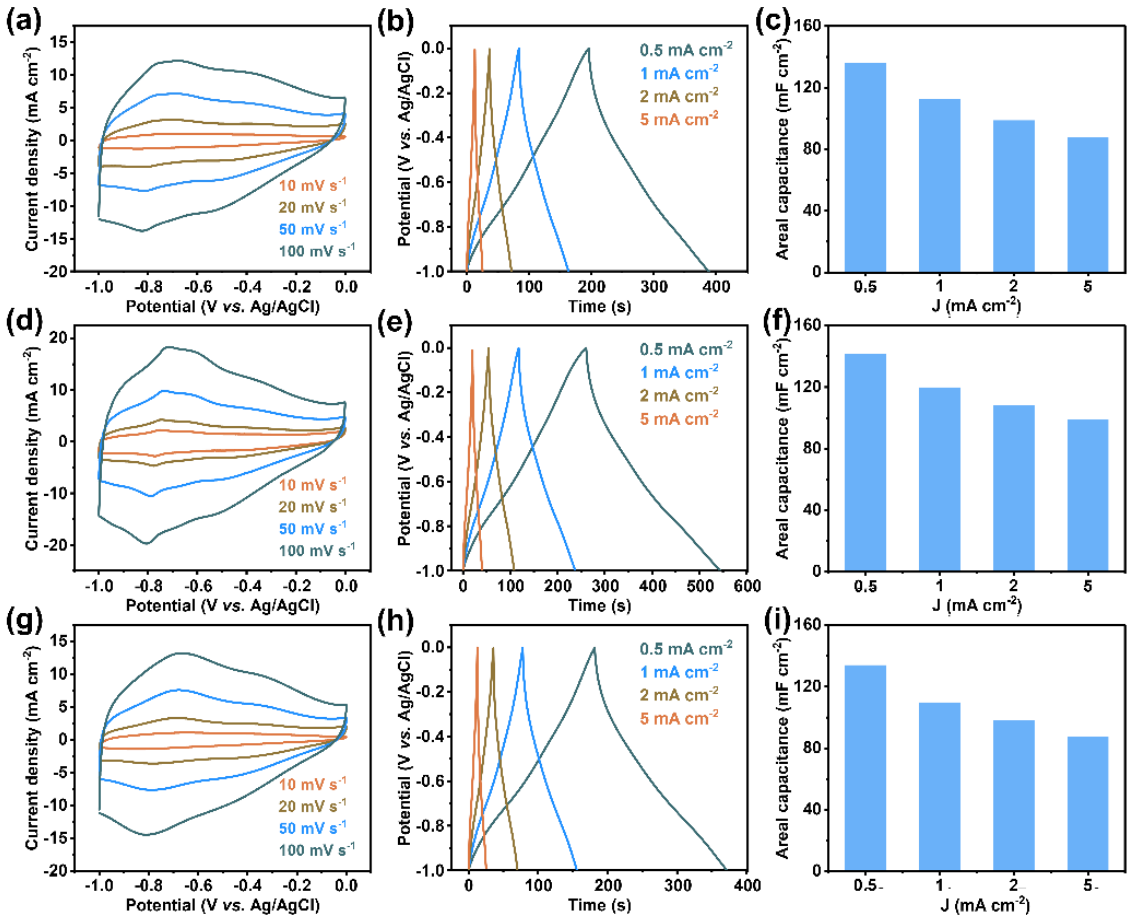

Fig. S13 CV curves at different scan rates, GCD curves at various current densities and areal capacitances at different current densities of VN electrodes sputtered at N_2 flow rate of (a-c) 5 scmm, (d-f) 7.5 sccm and (g-i) 10 scmm.

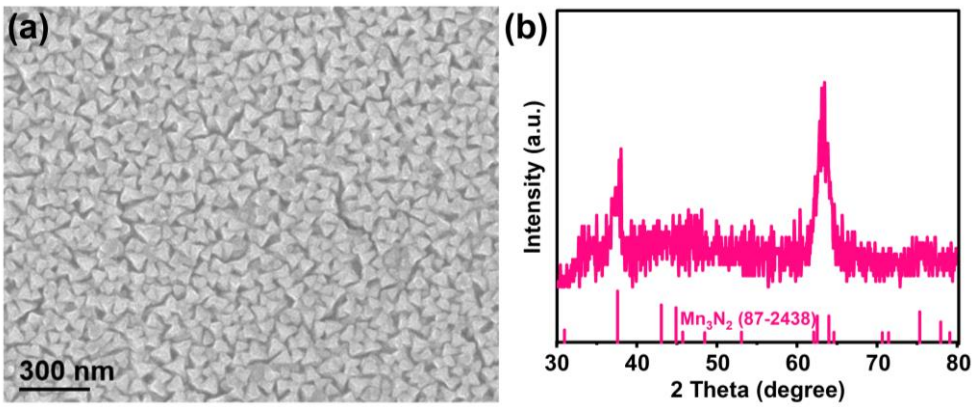

Fig. S14 (a) Surface SEM image and (b) XRD pattern of Mn_3N_2 thin film electrodes after cycling.

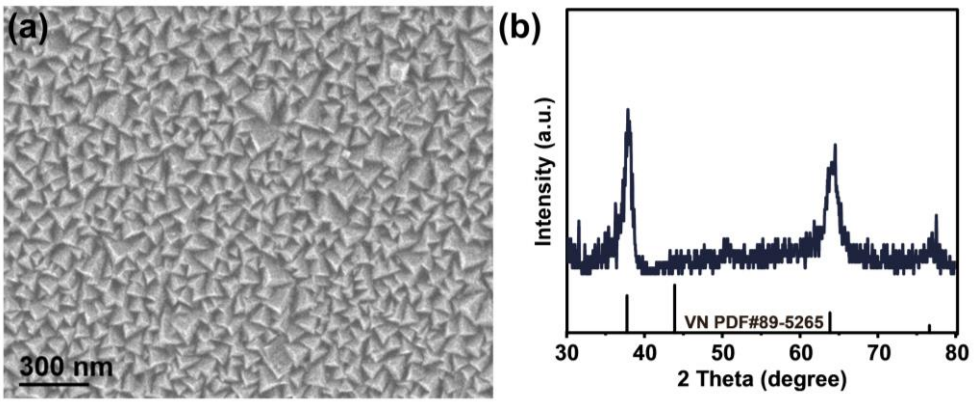

Fig. S15 (a) Surface SEM image and (b) XRD pattern of VN thin film electrodes after cycling.

Table S1 Comparisons of specific capacitance between Mn_3N_2 and recently reported TMNs-based electrodes.

Electrodes	Electrolyte	Specific capacitance	References
Mn_3N_2 thin film	1.0 M KOH	66.7 mF cm^{-2} at 1.0 mA cm^{-2} 952.8 F cm^{-3} at 1.0 mA cm^{-2}	This work
CrVN thin film	1.0 M KOH	30.6 mF cm^{-2} at 0.5 mA cm^{-2}	[10]
VN nanorod	1.0 M KOH	267.7 F cm^{-3} at 10 A cm^{-3}	[11]
TiN NTA	1.0 M LiOH	69.05 mF cm^{-2} at 0.3 mA cm^{-2}	[12]
TiN thin film	3.0 M KOH	21.8 mF cm^{-2} at 1.0 mA cm^{-2}	[13]
Ti-TiN films	3.0 M KOH	45.0 mF cm^{-2} at 1.0 mA cm^{-2}	[14]
TiN thin film	0.5 M H_2SO_4	205.1 F cm^{-3} at 1.0 mA cm^{-2}	[15]
CrVN thin film	0.5 M H_2SO_4	22.8 mF cm^{-2} at 1.0 mA cm^{-2}	[16]
Nb@NbN	0.5 M H_2SO_4	53.3 mF cm^{-2} at 1.0 mA cm^{-2}	[17]
CrN-Au	0.5 M H_2SO_4	56.8 mF cm^{-2} at 1.0 mA cm^{-2}	[18]
Mo-W-N nanocomposite	1.0 M Na_2SO_4	59.7 mF cm^{-2} at 1.0 mA cm^{-2}	[19]
Ni-Mo-N	1.0 M Na_2SO_4	43.11 mF cm^{-2} at 0.5 mA cm^{-2}	[20]
TiVN thin film	1.0 M Li_2SO_4	18.82 mF cm^{-2} at 0.1 mA cm^{-2}	[21]
Ti-Cr-N	1.0 M Li_2SO_4	63 mF cm-2 at 0.05 mA cm^{-2}	[22]
TiN film	1.0 M KCl	2.25 mF cm^{-2} at 0.15 mA cm^{-2}	[23]

Table S2 Comparisons of energy density and power density between Mn_3N_2//VN and other recently reported TMNs-based supercapacitor devices.

Electrodes	Electrolyte	Energy density (mWh cm^{-3})	Power density (W cm^{-3})	References
Mn_3N_2//VN	1.0 M KOH	153.1	53.7	This work
VN//$Co(OH)_2$-PHMSs//VN//$Co(OH)_2$-PHMSs	1.0 M KOH	19.7	2.064	[24]
CrVN//CrVN	0.5 M H_2SO_4	11.2	7.5	[16]
Nb@NbN//VN	0.5 M H_2SO_4	49.8	82.0	[17]
Mo-W-N//Mo-W-N	1.0 M Na_2SO_4	39.0	30.0	[19]
TiVN//TiVN	1.0 M Li_2SO_4	7.9	10.1	[21]
TiN/TiO_xN_y// TiN/TiO_xN_y	1.0 M KCl	0.7	359.0	[25]
W_2N//TiN	1.0 M Na_2SO_4	34.3	17.3	[26]
VN//VN	1.0 M KOH	40.8	0.5	[27]

References

[1] S.J. Clark, M.D. Segall, C.J. Pickard, P.J. Hasnip, M.J. Probert, K. Refson and M.C. Payne, First principles methods using CASTEP. *Z. Krist.* 2005, **220**, 567-570.

[2] J.P. Perdew, K. Burke and M. Ernzerhof, Generalized gradient approximation made simple. *Phys. Rev. Lett.* 1996, **77**, 3865.

[3] B. Hammer, L.B. Hansen and J.K. Nørskov, Improved adsorption energetics within density-functional theory using revised Perdew-Burke-Ernzerhof functionals. *Phys. Rev. B* 1999, **59**, 7413.

[4] G. Kresse and D. Joubert, From ultrasoft pseudopotentials to the projector augmented-wave method. *Phys. Rev. B* 1999, **59**, 1758.

[5] A. Kędziorski and M.C. Muñoz, Magnetic configuration, electronic structure, and stability of the low-index surfaces of η-Mn_3N_2: A first-principles study. *Phys. Rev. B* 2012, **86**, 155455.

[6] A. Tkatchenko and M. Scheffler, Accurate molecular van der waals interactions from ground-state electron density and free-atom reference data. *Phys. Rev. Lett.* 2009, **102**, 073005.

[7] R.S. Mulliken, Electronic population analysis on LCAO-MO molecular wave functions. I. *J. Chem. Phys.* 1955, **23**, 1833-1840.

[8] G, Henkelman, B.P. Uberuaga and H. Jónsson, A climbing image nudged elastic band method for finding saddle points and minimum energy paths. *J. Chem. Phys.* 2000, **113**, 9901-9904.

[9] M.M. Jiang, J. Xu, P. Munroe, Z.-H. Xie and Z.F. Chen, Light metal decorated graphene-like Si_2BN monolayers as hydrogen storage media: A DFT investigation. *Int. J. Hydrogen Energy* 2024, **50**, 865-878.

[10] D. Govindarajan, K. Parasuraman, M. Thandavarayan, T. Jayaraman, V. K. Ponnusamy and H.-S. Kim, Influence of chromium content on microstructural and electrochemical supercapacitive properties of vanadium nitride thin films developed by reactive magnetron co-sputtering process. *Ceram. Int.* 2019, **45**, 12643-12653.

[11] X.-L. Li, H. Song, Y.-H. Zhang, Y.-L. Ren, Q.-F. Guo, Z.-H. Tang, Z. Li, B. Gao. P.K. Chu, K.-F. Huo, Capacitance decay mechanism of vanadium nitride supercapacitor electrodes in KOH electrolytes. *Rare Met.* 2025, **44**, 3909-3919.

[12] Y.B. Xie and F. Tian, Capacitive performance of molybdenum nitride/titanium nitride nanotube array for supercapacitor. *Mater. Sci. Eng. B* 2017, **215**, 64-70.

[13] M. Ahmed, N. Ahmed, H. Ahmad, S. Bashir, R. Subramaniam and G. Ali, A comparative study on exploring sputtered titanium nitride thin films for high-performance supercapacitors. *J. Energy Storage* 2025, **105**, 114712.

[14] N. Ahmed, M. Ahmed, H.B. Shahid, S. Bashir, R. Subramaniam and G. Ali, Advanced Ti-TiN thin films: Leveraging sub-stoichiometry for superior hybrid supercapacitor performance. *J. Power Sources* 2026, **665**, 238983.

[15] H.Y. Tong, Z.X.R. Nan, H.L. Zhang, B.B. Yang, Y.J. Liu, P.Q. Guo, Y.Y. Wei, Z.F. Zi and X.B. Zhu, Synthesis and performance of TiN film electrode for supercapacitor by a facile chemical solution deposition method. *J. Mater. Sci: Mater. Electron.* 2024, **35**, 182.

[16] B.B. Wei, J.G. Wu, Z. Hou, M.J. Fang, H.J. Zeng, X.T. Yan, Q.X. Guo, Y. Yang, Z.C. Wang and Z.Q. Qi, Binder-free V-doped CrN thin film electrode enables high performance symmetric supercapacitor. *J. Alloys Compd.* 2024, **977**, 173424.

[17] J.G. Wu, B.B. Wei, Q.X. Guo, H.J. Zeng, X.T. Yan, M.J. Fang, Y. Zeng, H.F. Liang and Z.B. Qi, Hierarchical Nb@NbN core-shell-like nanocolumns for asymmetric supercapacitors. *J. Colloid Interface Sci.* 2025, **679**, 391-400.

[18] P.S. Roy, A. Biswas, K. Bhattacharyya, S. Sarkar, V.B. Jayakrishnan and D. Bhattacharyya, High performance symmetric supercapacitors based on Au incorporated CrN thin films fabricated by reactive magnetron sputtering. *Electrochim. Acta* 2024, **498**, 144680.

[19] V. Lohan, R, Kumar, B. Ranjan, H. Rahman and D. Kaur, Harnessing synergy in reactively Co-sputtered Mo-WN pseudocapacitive nanocomposite for high-performance flexible Na-ion supercapacitor. *J. Power Sources* 2026, **662**, 238775.

[20] B. Ranjan and D. Kaur. Pseudocapacitance powered nickel molybdenum nitride nanocomposite reactively cosputtered on stainless-steel mesh toward advanced flexible supercapacitors. *ACS Appl. Energy Mater.* 2024, **7**, 4513-4527.

[21] S. Issar, S. Kodan, A. Bansal, A. Tomar, N. Choudhary and R. Chandra, Li-salt assisted high performance bimetallic titanium vanadium nitride-based symmetric supercapacitor device for energy storage application. *Electrochim. Acta* 2025, **535**, 146636.

[22] R. Kumar, B. Ranjan, K. Kumar, S. Shankhdhar and D. Kaur, Ti-Cr-N nanopyramid/nitrogen-doped carbon quantum dot/stainless steel mesh as a flexible supercapacitor electrode. *ACS Appl. Nano Mater.* 2024, **7**, 7663-7673.

[23] J.X. Tan, L. Yi, M. Zhang and S.Y. Bai, Influence of N_2/Ar Flow ratio on the microstructure and electrochemical capacitive performance of TiN thin-film electrodes for micro-supercapacitors. *Coatings* 2026, **16**, 69.

[24] S. Wang, Z.-S. Wu, F. Zhou, X.Y. Shi, S.H. Zheng, J.Q. Qin, H. Xiao, C.L. Sun and X.H. Bao, All-solid-state high-energy planar hybrid micro-supercapacitors based on 2D VN nanosheets and Co $(OH)_2$ nanoflowers. *npj 2D Mater. Appl.* 2018, **2**, 7.

[25] N.N. Sun, J. Xu, Y.P. Su, P. Jiang, Y.Z. Zou, W.W. Liu, M.X. Wang and D.Y. Zhou, Energy storage performance of in-situ grown titanium nitride current collector/titanium oxynitride laminated thin film electrodes, *Chem. Eng. J.* 2023, **474**, 145603.

[26] R. Kumar, B. Ranjan and D. Kaur. Porous W_2N fibrous nanograins and TiN nanopyramid framework for high-energy density flexible asymmetric supercapacitors. *Appl. Phys. Lett.* 2025, **126**, 133902.

[27] X.-L. Li, H. Song, Y.-H. Zhang, Y.-L. Ren, Q.-F. Guo, Z.-H. Tang, Z. Li, B. Gao, P.K. Chu and K.-F. Huo, Capacitance decay mechanism of vanadium nitride supercapacitor electrodes in KOH electrolytes. *Rare Met.* 2025, **44**, 3909-3919.